



Normal and abnormal grain growth in fine-grained Nd-Fe-B sintered magnets prepared from He jet milled powders



F. Bittner^{a,b,*}, T.G. Woodcock^a, L. Schultz^{a,b}, C. Schwöbel^c, O. Gutfleisch^{c,d}, G.A. Zickler^e, J. Fidler^e, K. Üstüner^f, M. Katter^f

^a IFW Dresden, Institute for Metallic Materials, PO Box 270116, 01171 Dresden, Germany

^b Technische Universität Dresden, Institute of Materials Science, 01062 Dresden, Germany

^c Technische Universität Darmstadt, Materialwissenschaft, Alarich-Weiß-Str. 16, 64287 Darmstadt, Germany

^d Fraunhofer ISC, Projektgruppe für Werkstoffkreisläufe und Ressourcenstrategie IWKS, Rodenbacher Chaussee 4, 63457 Hanau, Germany

^e Technische Universität Wien, Institute of Solid State Physics, Wiedner Hauptstr. 8-10, 1040 Wien, Austria

^f Vacuumschmelze GmbH & Co. KG, 63412 Hanau, Germany

ARTICLE INFO

Keywords:

Nd-Fe-B

Permanent magnet

Abnormal grain growth

Coercivity

Electron backscatter diffraction

ABSTRACT

Fine-grained, heavy rare earth free Nd-Fe-B sintered magnets were prepared from He jet milled powders with an average particle size of 1.5 μm by low temperature sintering at 920 °C or 980 °C. A coercivity of > 1600 kA/m was achieved for an average grain size of 1.68 μm . Transmission electron microscopy showed that the distribution and composition of intergranular and grain boundary junction phases was similar to that in conventionally processed magnets. Microstructural analysis on different length scales revealed the occurrence of abnormal grain growth, which is unexpected for sintering temperatures below 1000 °C. A larger area fraction of abnormal grains was observed in the sample sintered at 920 °C compared to that sintered at 980 °C. Microtexture investigation showed a better crystallographic alignment of the abnormal grains compared to the fine-grained matrix, which is explained by a size dependent alignment of the powder particles during magnetic field alignment prior to sintering. Slightly larger particles in the initial powder show a better alignment and will act as nucleation sites for abnormal grain growth. Magneto-optical Kerr investigations confirmed the lower switching field of the abnormal grains compared to the fine-grained matrix. The demagnetisation curve of the sample sintered at 920 °C showed reduced rectangularity and this was attributed to a cooperative effect of the larger fraction of abnormal grains with low switching field and, as a minor effect, a reduced degree of crystallographic texture in this sample compared to the material sintered at 980 °C, which did not show the reduced rectangularity of the demagnetisation curve.

1. Introduction

Nd-Fe-B permanent magnets have many different applications as their extrinsic magnetic properties, coercivity H_c and remanent polarisation J_r , can be adjusted over a wide range [1,2]. There is a growing demand for magnets suitable for use in electric motors with working temperatures up to 200 °C and these require room temperature coercivities > 1600 kA/m [1,2]. Coercivity is an extrinsic property i.e. it depends on intrinsic properties, in this case the anisotropy field of the 2:14:1 phase, and also on the microstructure [3]. Thus two different approaches are possible to increase H_c . Partial substitution of Nd by heavy rare earth (HRE) elements will increase the anisotropy field of the 2:14:1 phase remarkably [4] and coercivities of 2400 kA/m are achievable if 4 at% Dy are added [1,2], however, HRE elements are

critical in terms of their availability [5] and are therefore much more expensive than Nd [6].

The second approach concerns increasing coercivity by microstructural optimisation, for example, the role of grain size on coercivity in Nd-Fe-B based permanent magnets was investigated by several authors [7–12]. It was found that sintered magnets with coercivity of more than 2000 kA/m are achievable without the usage of any HRE elements if the average grain size could be reduced to 1 μm [11,12].

Nd-Fe-B based magnets are produced by a powder metallurgical route, whereby the grain size of the sintered magnet depends on the particle size of the initial powder and on the sintering conditions. Nd-Fe-B powders are commonly produced by jet milling in nitrogen, which results in a minimum particle size of 2–3 μm [11,12]. The minimum particle size for a jet milled powder depends strongly on the circumfer-

* Corresponding author at: IFW Dresden, Institute for Metallic Materials, PO Box 270116, 01171 Dresden, Germany.
E-mail address: f.bittner@ifw-dresden.de (F. Bittner).

ential speed inside the mill [13] which can, accordingly to the kinetic theory of gases, be increased by using He instead of N₂. The production of sintered Nd-Fe-B magnets from He jet milled powder was demonstrated [14,15] and a remarkable increase of coercivity from 1250 kA/m to 1590 kA/m was achieved for a reduction of the initial powder particle size from 2.7 μm to 1.1 μm [15]. One disadvantage of the magnets produced by this method was that the shape of the demagnetisation curve was less rectangular than that of sintered magnets processed from powders obtained by N₂ jet milling [15,16].

The reduction of the initial powder particle size can only contribute to an enhancement of H_c if a homogenous fine-grained microstructure is preserved after sintering. Nd-Fe-B sintered magnets are conventionally sintered at temperatures between 1050 and 1100 °C [17]. At such high temperatures grain growth will take place, resulting in a homogenous coarsening of the microstructure [18,19] and therefore the average grain size after sintering is significantly larger than the particle size of the precursor powder [11,12]. Powders with smaller particle size will show a higher tendency for such grain growth due to their larger specific surface area. Furthermore, abnormal grain growth can be observed in Nd-Fe-B sintered magnets [20]. Abnormal grain growth is thought to be responsible for a significant deterioration of the magnetic properties such as coercivity [20,21] and rectangularity of the demagnetisation curve [8,22]. Several factors promoting this rapid and discontinuous growth of certain grains such as sintering temperature, particle size and size distribution and degree of alignment have been reported [22–26] but no conclusive mechanism was proposed so far.

The aims of this work are to study the normal and abnormal grain growth in Nd-Fe-B sintered magnets produced from He jet milled powder and to investigate the loss of rectangularity in the demagnetisation curves in such materials. A detailed microstructural characterisation on different length scales will be presented including scanning electron microscopy (SEM), electron backscatter diffraction (EBSD), magneto-optical Kerr microscopy and transmission electron microscopy (TEM). Microstructural differences appearing during sintering are analysed quantitatively and their impact on the magnetic properties is discussed with the major focus lying on the importance of grain size and size distribution and the local crystallographic orientation of the individual grains.

2. Experimental

Two HRE free powders with the compositions (Nd,Pr)_{14.99}Fe_{76.05}TM_{3.25}B_{5.71} for Powder A and (Nd,Pr)_{17.02}Fe_{74.18}TM_{3.19}B_{5.61} for Powder B with TM=Al, Ga, Co, Cu were produced by He jet milling. The average particle size was determined according to a Fisher Sub Sieve Sizer (F.S.S.S.) and the particle size distribution was determined by Laser diffraction method using a class width of 0.1 μm. F.S.S.S. is based on the measurement of the drop of air pressure, if an airflow of constant initial pressure is passed through a powder sample. Two magnets were produced from the powders by alignment under an applied magnetic field of 1300 kA/m, cold-pressing, and sintering. Magnet A was obtained from Powder A by sintering at 980 °C and Magnet B which was made from Powder B was sintered at 920 °C. The higher Nd content of powder B was designed to allow full densification of Magnet B at this low sintering temperature and the density was determined using Archimedes' principle. Both magnets were post sinter annealed at 500 °C. The magnetic properties were measured using a hysteresisgraph with maximum reversal field of 1600 kA/m. For the microstructural investigations the samples were ground and polished using a standard metallographic procedure. The microstructure was studied using a Gemini Leo 1530 Scanning Electron Microscope (SEM). The local crystallographic orientation was determined by electron backscattered diffraction (EBSD) measurements. For mapping, an evenly spaced grid of measurement points was chosen in the analysis region and the spacing was 0.3 μm. The global texture was determined by EBSD with a

spacing of 1 μm and collecting the orientation of more than 10,000 individual grains for each sample. The grain size of the sintered magnets was measured using the linear intercept method and more than 2500 grains were analysed for each sample. To determine the number and fraction of abnormal large grains SEM images with low magnification representing 3% (2.4 mm²) of the entire magnet cross section were used in combination with the linear intercept method. According to the fundamental principals of stereology, the volume fraction of abnormal large grains is equal to their area fraction.

The nanoanalytical investigations were carried out on an analytical field emission transmission electron microscope (TEM) (FEI Tecnai F20) operating at 200 kV, which is equipped with a silicon drift energy dispersive X-ray detector (EDX) from EDAX, a Gatan Tridem GIF electron energy loss spectrometer (EELS) and a high angle annular dark field detector (HAADF). The EELS cross-sections of Pr and Nd relative to Fe, were obtained with Pr₂Fe₁₄B and Nd₂Fe₁₄B standards. TEM specimens were prepared in a FEI Quanta 200 3D DualBeam – Focused Ion Beam (FIB) using the lift-technique.

The magneto-optical Kerr (MOKE) images of polished samples were taken on a Zeiss Axio Imager.D2m microscope equipped with a polarized light function. Measurements were done using the polar component of the reflected light and to reduce the topological effects a subtraction method was used. An external field was applied using a rotatable Halbach-array providing a field of 1 T.

3. Results and discussion

3.1. Microstructure of fine-grained sintered magnets

The particle size distribution of the He jet milled Powder A was determined using laser diffraction method and is shown in Fig. 1. No significant differences in the particle distribution were observed between Powder A and B. The average particle size was 1.5 μm according to F.S.S.S. and 2 μm according to laser diffraction. The obtained powder is remarkably finer than powder produced by N₂ jet milling, which has average particle size between 2.7 and 3 μm [11,15]. This makes the He jet milled powder a promising prematerial for the fabrication of fine-grained sintered magnets. The particle size distribution can be quantified using the ratio D90/D10, where D90 corresponds to the mesh size (particle diameter) for passing of 90 wt% of the powder and D10 corresponds to the mesh size (particle diameter) passing of 10 wt% of powder particles. In the current study a distribution width D90/D10≈2.5 was evaluated and from this finding it can be excluded that particles with diameters larger than 10 μm were present before sintering. This value will be used later to distinguish between fine-grained majority and abnormal grown grains.

The microstructure of the sintered magnets is shown in Fig. 2(a)

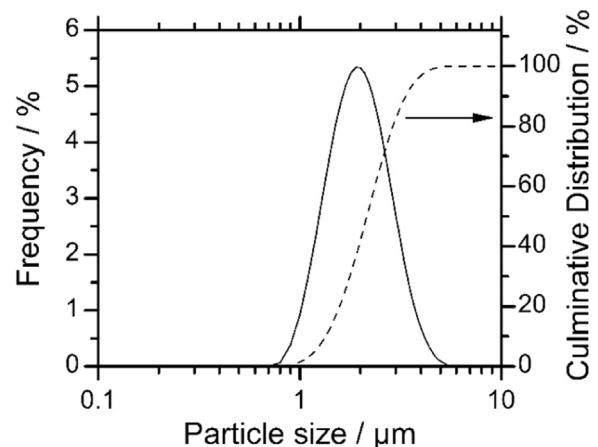


Fig. 1. Particle size distribution of the He jet milled Powder A.

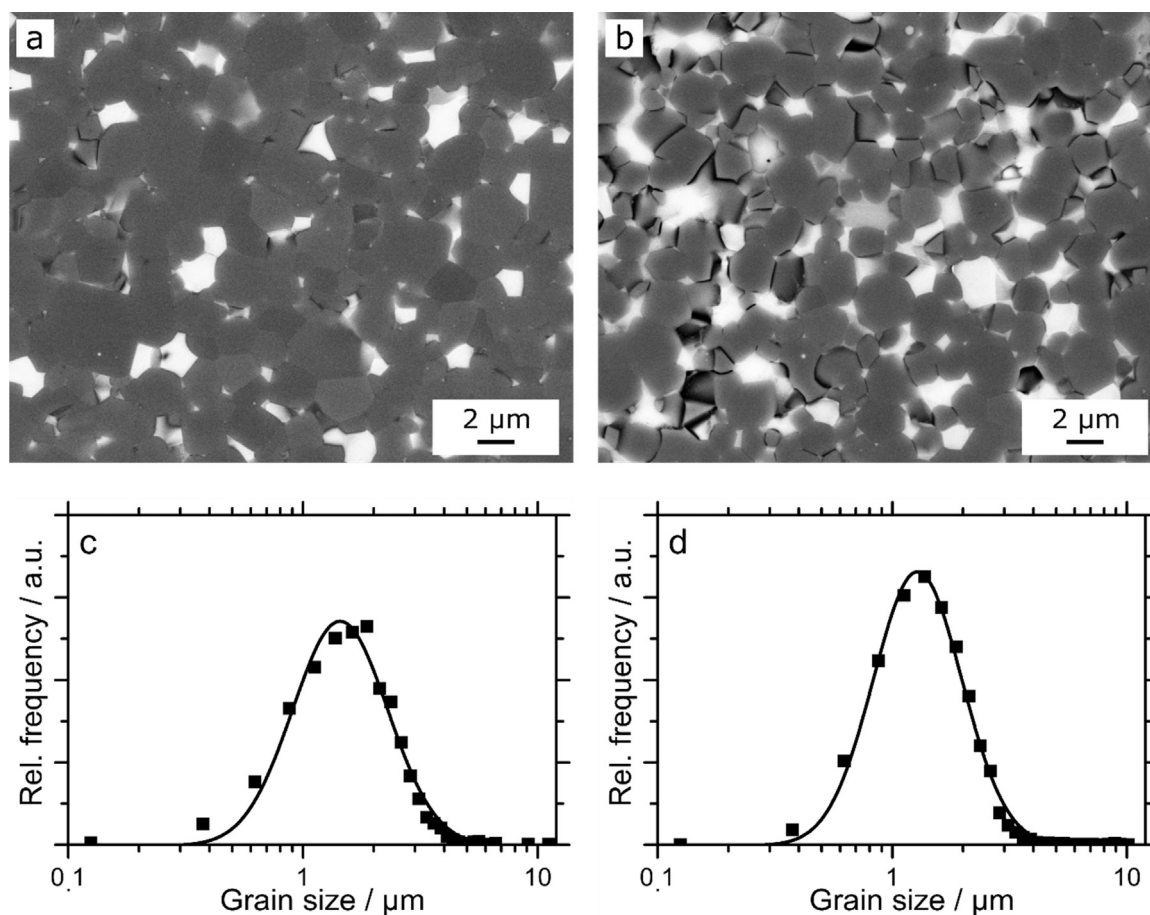


Fig. 2. Microstructure and 2:14:1 grain size distribution of Magnet A (a,c) and Magnet B (b,d). The grain size distributions were obtained from the linear intercept method with a class width of 0.25 μm . Black lines correspond to a fitted log-normal distribution of the grain size.

and (b). The grains of the hard magnetic 2:14:1 phase appear grey while the bright particles are Nd-rich phases. Both magnets show a fine-grained microstructure with a 2:14:1 grain size below 2 μm . It is apparent that the Nd-rich grains have almost the same size as the 2:14:1 grains. The density of the magnets was determined to be 7.59 and 7.58 g/cm^3 for Magnet A and B, respectively, which is very close to the density of $\text{Nd}_2\text{Fe}_{14}\text{B}$ (7.6 g/cm^3 [27]). The intergranular cohesion seems to be reduced in Magnet B, possibly due to the low sintering temperature, which results in the falling out of some grains during the preparation. This effect is visible as porosity in Fig. 2(b).

The mean linear intercept grain size was $1.95 \pm 0.06 \mu\text{m}$ and $1.69 \pm 0.03 \mu\text{m}$ for Magnet A and Magnet B, respectively. Both samples are fine-grained but Magnet B has a slightly smaller mean grain size which is likely to be because of the lower sintering temperature compared to Magnet A. The mean grain size of Magnet B is very close to the average particle diameter of the He jet milled powder (1.5 μm). The small difference may be attributed to the different measuring methods. It is concluded that no normal grain growth appears for the fine powder B if it is sintered at 920 $^\circ\text{C}$. In contrast, the slightly higher grain size in Magnet A indicates that some normal grain growth occurs in this composition if the sintering temperature is 980 $^\circ\text{C}$.

The grain size distributions obtained from quantitative metallography for both magnets are shown in Fig. 2(c) and (d). The frequencies are normalised to the total number of grains for each magnet. Both magnets display a log-normal distribution of the grain size which is shown as a black line in both diagrams.

Besides the normal grain growth during sintering which affects the fine-grained majority of grains, some much larger grains with diameters ranging from 10 to 100 μm are observed in both magnets. This phenomenon is known as abnormal grain growth and Fig. 3 shows an

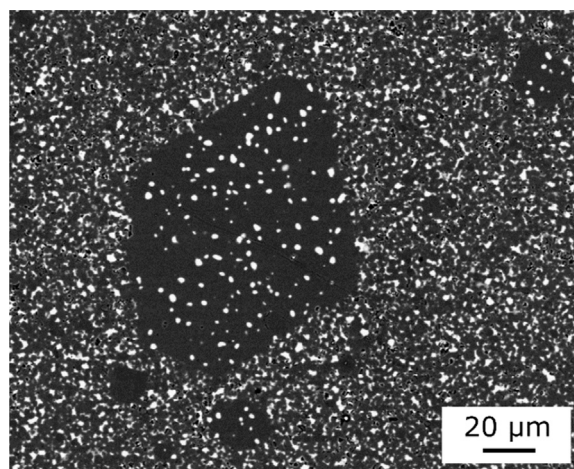


Fig. 3. SEM image of Magnet B showing one abnormal large grain in the fine grained microstructure.

example including one grain with a size of 80–100 μm and some grains with diameters of 10–20 μm . They are embedded into the fine-grained microstructure with homogenous distribution of 2:14:1 and Nd-rich grains. No abnormal grains larger than 100 μm were observed in this study. This is substantially smaller compared to conventionally prepared sintered magnets [20]. From Fig. 3 it can be seen that abnormal grains contain spherical shaped Nd-rich particles. The formation mechanism of these inclusions may be proposed as follows. During the sintering process, the Nd-rich grains located at the triple points melt. These pockets of Nd-rich liquid become trapped inside the

Table 1
Mean grain size, number and area fraction of large grains in Magnet A and B.

Magnet	Mean grain size	Number of grains > 10 μm	Area fraction of grains > 10 μm
A	$1.95 \pm 0.06 \mu\text{m}$	$65 \pm 5 \text{mm}^{-2}$	0.99%
B	$1.69 \pm 0.03 \mu\text{m}$	$130 \pm 6 \text{mm}^{-2}$	1.68%

abnormal grains and, on cooling, they solidify as spherical particles. This special morphology was also discussed elsewhere [24].

Abnormal grain growth is a well-known problem for Nd-Fe-B based sintered magnets and it leads to the formation of a bimodal grain size distribution [28]. The fact that a lowering of the sintering temperature leads to an increased number and area fraction of abnormal grains is in contradiction to previous studies, where an onset temperature of more than 1050 °C was required to activate the discontinuous coarsening of the microstructure [24,26]. This was explained by the need to form nuclei with critical diameter by normal grain growth before these grow abnormally [24]. A reduction of the average grain size and a broad particle size distribution can lower the critical temperature by some tens of degrees [26] but the occurrence of abnormal grain growth was not reported for sintering temperatures below 1000 °C so far. The occurrence of abnormal grain growth at the sintering temperatures used here (920 °C and 980 °C) is therefore interesting.

The number and fraction of grains with a diameter > 10 μm was determined and the results of the quantitative metallography for both magnets are summarized in Table 1. It can be seen that the low temperature sintered Magnet B shows a higher tendency for abnormal grain growth; the number and fraction of abnormal grains is significantly lower in Magnet A.

As discussed above, abnormal grain growth requires a nucleus of critical size. In the present case the sintering temperature was chosen to be very low in an attempt to avoid both normal and abnormal grain growth. Formation of such nuclei by normal grain growth therefore seems to be unlikely since the average grain size was not much increased in either composition. The size distribution of the He jet milled powder (Fig. 1) is narrow ($D_{90}/D_{10} \approx 2.5$) but some particles with a diameters up to 3–5 μm may still be present in the initial powder with a low frequency. If these few larger grains act as nuclei, this could explain why abnormal grain growth is found at these low sintering temperatures. As the particle size distribution in both starting powders was identical, the larger number of abnormal grains in Magnet B is likely to be due the difference in composition, i.e. Magnet B has a higher RE-content and therefore a higher amount of liquid phase during sintering is expected. Furthermore a higher amount of 2:14:1 phase will be dissolved in the liquid. These effects are likely to promote abnormal grain growth.

Morphological maps of the FIB lamella from Magnet A and B show the granular microstructure obtained by the structural investigation via selected area electron diffraction (SAED) and fast fourier transformation (FFT) of high resolution TEM/STEM (HRTEM) (Fig. 4(a)). The hard magnetic 2:14:1 phase with lattice parameter $a=0.8805 \text{nm}$ and $c=1.2206 \text{nm}$ and space group no. 136 [29] is coloured in grey (Fig. 4(a)).

The majority of the grain boundary junctions (GBj) were identified as $c\text{-(Pr,Nd)}_2\text{O}_3$ (red in Fig. 4(a)) ($a=1.108 \text{nm}$, space group no. 206 [30]). This phase occurs at most intersections, where more than two grains meet. Although the rare earth (RE) content of Magnet B is more than 2 at% higher than in Magnet A, the volume fraction of this GBj phase is nearly the same in both magnets. The majority of the excess RE in Magnet B is agglomerated in a RE rich grain like fcc-(Pr,Nd)O phase (blue in Fig. 4(a)) ($a=0.4994 \text{nm}$, space group no. 225 [31]). These phases were also reported by several other authors [32–38]. A fcc-(Pr,Nd)O phase surrounded by four 2:14:1 grains from the central area of the FIB sample of Magnet A (Fig. 4(a)) is displayed in a HAADF

image (Fig. 4(b)). EELS investigations have shown a residual Fe content of approximately 10 at% in the $c\text{-(Pr,Nd)}_2\text{O}_3$ phase and no Fe at all in the fcc-(Pr,Nd)O phase.

A typical grain boundary (GB) with a thickness of 3.5 nm, where the misorientation angle θ_0 of the [001] directions of the two adjacent grains is 16°, is shown in the HRTEM image (Fig. 4(c)). The difference in the GB thickness of Magnet A (2.7 nm) and Magnet B (3.4 nm) is in the order of the error size of the measurement. The relative chemical composition across an EELS line scan from one 2:14:1 grain over a GB into another grain attributes the GB to consist mainly of RE (Pr+Nd), TM (Fe+Co) and a smaller amount of O and F (Fig. 4(d)). The quantitative oxygen content in the EELS line scan was corrected due to surface oxidation caused by sample preparation and labeled O*. The reason for finding F within in the grain boundary is not clear since no F was added during magnet fabrication or preparation.

The wetting behaviour of the liquid phase during sintering is influenced by dopants like Al, Ga and Cu [39]. We only identified an Al-containing phase, such as $\text{Nd}_6\text{Fe}_{13}\text{Al}$, near GBjs in the investigated magnets occasionally. The minor nominal content of Ga and Cu (< 0.4 at%) was too low to form separate phases. These dopants were equally distributed in the intergranular and hard magnetic phases.

Numerical Monte Carlo simulations using the software package 3D CASINO v 3.2 [40] on the electron beam broadening in an $\text{Nd}_2\text{Fe}_{14}\text{B}$ sample were conducted in order to determine the spatial resolution of EELS experiments, in specific the ratio of the GB volume illuminated from the electron beam with respect to the illuminated volume of the surrounding grains. The electron beam broadening due to the conical beam shape, elastic and inelastic scattering events is negligible for a minimal beam diameter of 1.5 nm and a semi-convergence angle of 6 mrad.

The orientation of the GB plane with respect to the incident electron beam is the crucial parameter determining the quality of the chemical information of the GB. At a tilt angle of the GB plane with respect to the incident electron beam of 5° and a sample thickness of 50 nm the illuminated volume from the surrounding grains is approximately 20%. Since the 2:14:1 phase consists to 82.4 at% of Fe, this illuminated volume of the grain causes a rise in the Fe concentration in the GB. Therefore the Fe at% in the GB has to be reduced by 5–10 at%, because it is not possible to determine the orientation of the GB plane with a much smaller angle than 5°. The influence of the GB tilt is reduced with smaller sample thicknesses and it is therefore important to have a region of the TEM specimen with a thickness < 50 nm. The much higher yield of the inelastic scattering events in EELS with respect to EDX has a great advantage for the analysis of the chemical composition of thin GBs. Only a few percent of the isotropic emitted characteristic X-rays can be detected by the EDX detector however the collection efficiency of the electron spectrometer in EELS experiments is typically in the range of 20–50% [41]. Another advantage is the higher energy resolution of EELS (dispersion used: 0.3 eV/ch) over EDX (10 eV/ch). The chemical composition of the GB of both samples is comparable and the Fe content is ranging between 40 and 60 at%, which is in good agreement with recent 3D atom probe [14,42] and TEM/STEM experiments [43] on similar materials and STEM experiments on nanocrystalline Nd-Fe-B materials [44]. The high Fe content in the GB phase implies that this phase may have soft-ferromagnetic properties. Spin-polarized SEM and electron holographic TEM experiments accredit the GB phase to be soft-ferromagnetic with a saturation polarisation of 0.5–1.0 T [45,46]. Micromagnetic finite element simulations show the significant influence of the magnetic properties of the GB phase on the coercivity of sintered Nd-Fe-B magnets [47,48]. Only with soft-ferromagnetic GB properties the resulting coercive field is comparable to experimental values. The soft-ferromagnetic GB phase leads to a magnetic coupling of the hard magnetic 2:14:1 grains and therefore to a significant reduction of the coercive field [49].

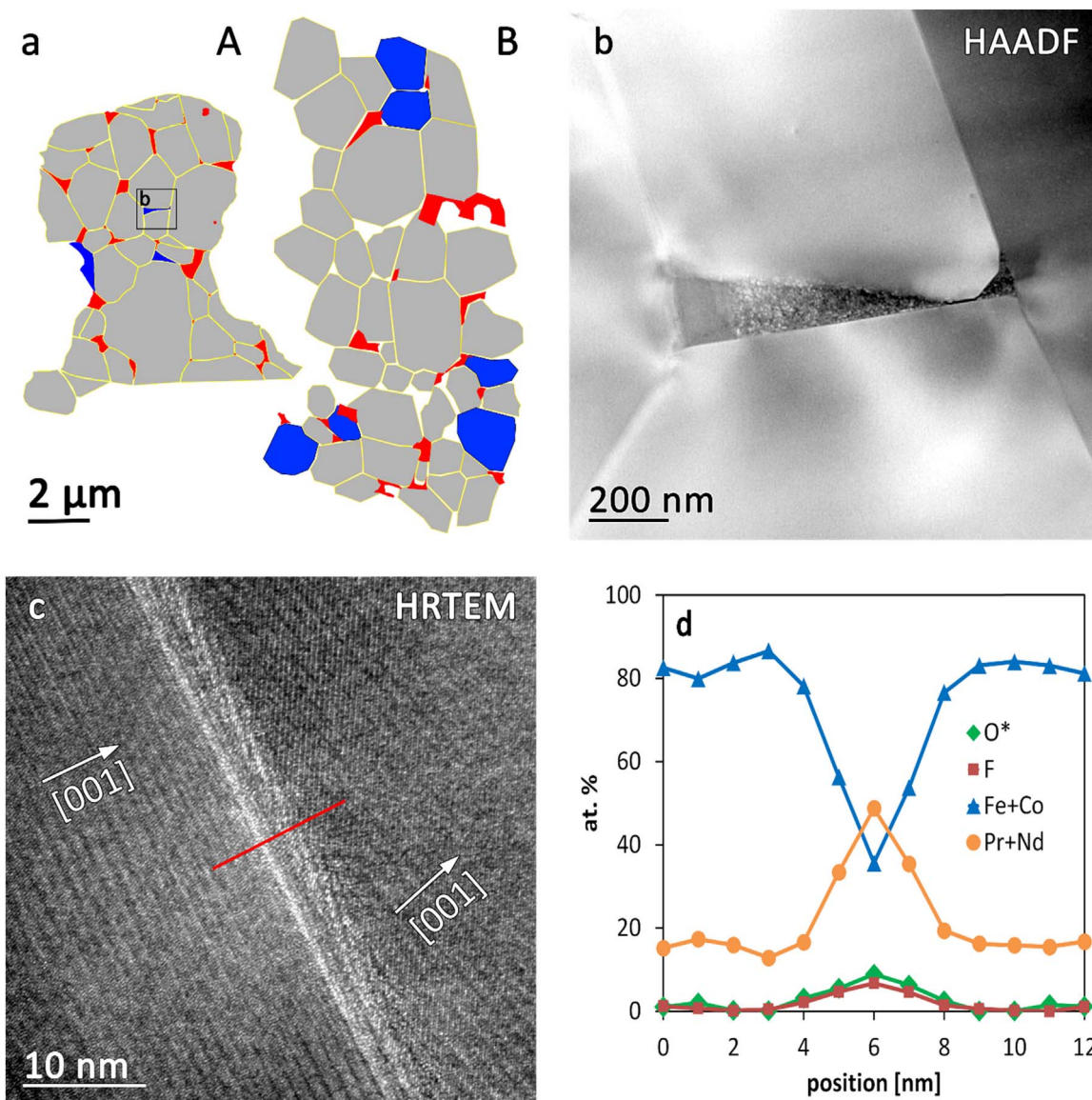


Fig. 4. a) Morphological maps of the occurring phases of FIB samples of magnet A and B, grey=(Pr, Nd)₂(Fe,Co)₁₄B, red=c-(Pr,Nd)₂O₃, blue=(Pr,Nd)O; b) HAADF image of a (Pr,Nd)O GBj surrounded by four 2:14:1 grains; c) HRTEM image of two adjacent 2:14:1 grains with an misorientation of 16° ([001] lattice fringes) are separated by an 3.5 nm thick RE rich GB; d) EELS line scan across the RE-rich GB (red line in (c)). (For interpretation of the references to color in this figure legend, the reader is referred to the web version of this article.)

3.2. Global and local texture investigations

The texture of both magnets was analysed using the EBSD sampling method i.e. the orientation of a large number of grains (in this case more than 10,000 in each sample) was measured. As a consequence of the large number of grains the orientation data is comparable to that returned by other macrotexture measurement techniques e.g. x-ray diffraction [50,51]. The 001 pole figures of both magnets (not shown) prove that both magnets display a strong <001> fibre texture. The 001 pole density as a function of the angle from the sample normal direction is plotted for both magnets in Fig. 5. The results are histograms with 5° binning and the bin centres are plotted. In order to be able to compare both samples, the data on the y-axis have been normalised giving multiples of uniform pole density (M.U.D.), where M.U.D.=1 represents an isotropic sample (dashed line). Taking the M.U.D. value in the first bin (0–5°) as a measure of texture quality, it can be seen that the texture quality is lower in Magnet B than Magnet A. A similar trend was also observed by TEM measurements of the orientation of a small number of grains.

The local orientation of the individual 2:14:1 grains was mapped by

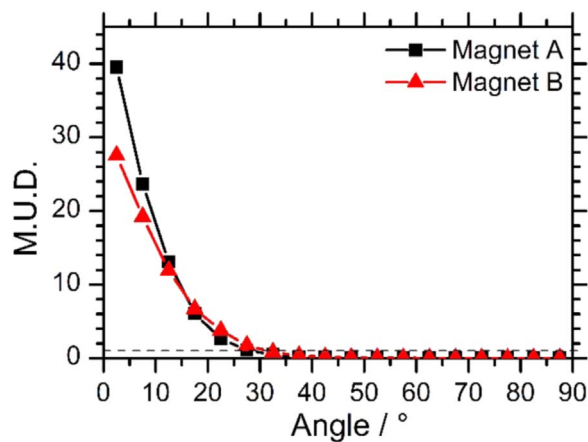


Fig. 5. Orientation histogram for Magnet A (black square) and Magnet B (red triangles) showing the (001) pole density in multiples of uniform pole density (M.U.D.) as a function of the angle from the sample normal using a class width of 5°. (For interpretation of the references to color in this figure legend, the reader is referred to the web version of this article.)

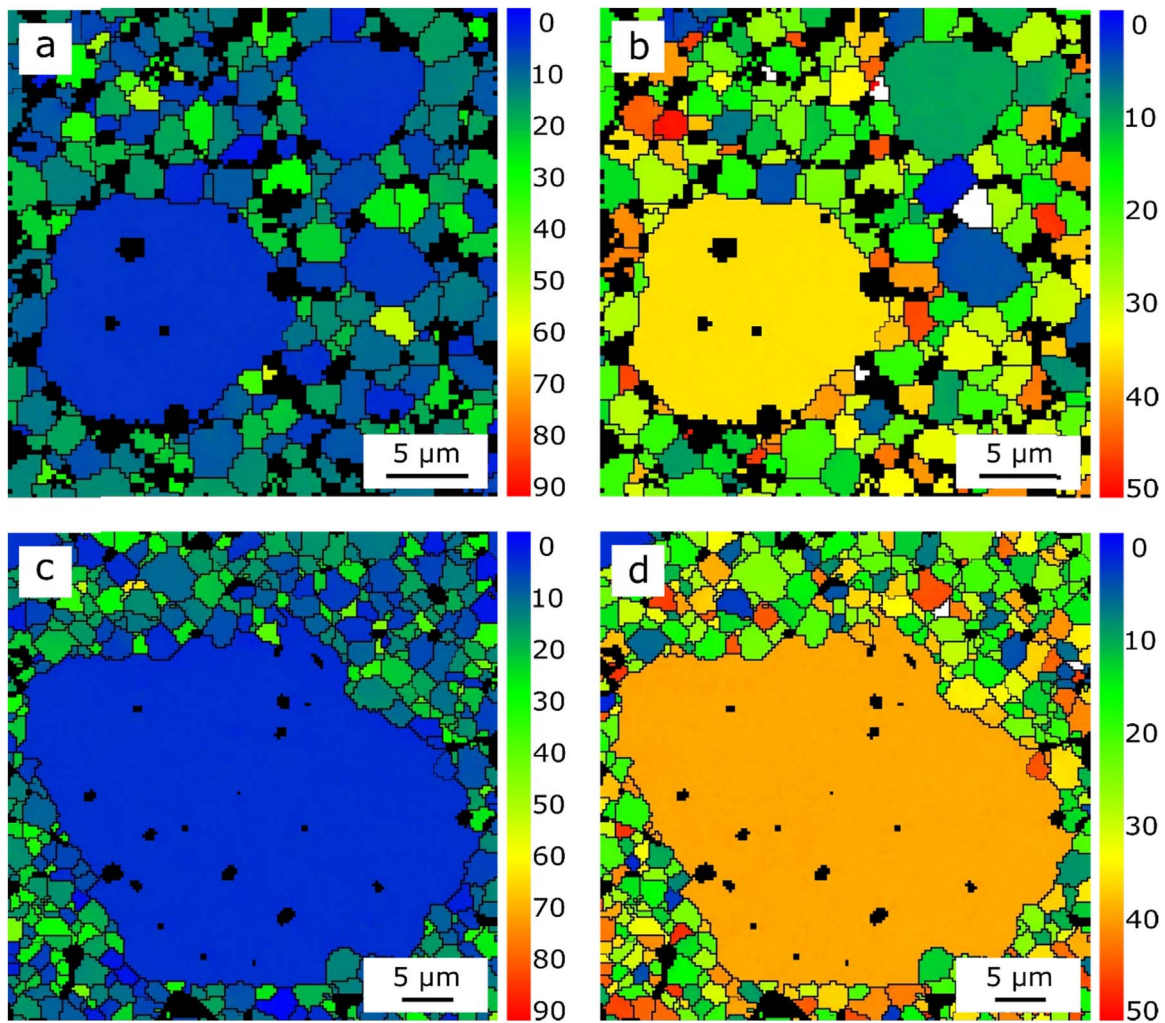


Fig. 6. EBSD maps of Magnet B in the out of plane (a,c) and in plane orientation (b,d) showing a large grain with $d > 10 \mu\text{m}$ (a,b) and an abnormal grown grain (c,d). (For interpretation of the references to color in this figure legend, the reader is referred to the web version of this article.)

EBSD using a step size of $0.3 \mu\text{m}$ and two regions showing different microstructural features are shown in Fig. 6(a), (b) and (c), (d), respectively. Fig. 6(a) and (c) display the out of plane orientation and the colour code represents the orientation of the crystallographic c -axis of the 2:14:1 phase parallel to the out of plane direction. Fig. 6(b) and (d) show the in-plane orientation, e.g. the angle between the crystallographic a -axis and the reference x -axis. The black pixels in Fig. 6 correspond to non-indexed microstructural features such as Nd-rich phases or pores. Both maps contain undesirable microstructural features, i.e. grains with diameters significantly larger than the average grain size. These grains are embedded into the fine-grained matrix. From the maps displaying the out of plane orientation (Fig. 6(a) and (c)) it can be seen that the 2:14:1 grains general have a good alignment of the crystallographic c -axis. Together with the in plane orientation maps (Fig. 6(b) and (d)) it can be concluded that the magnet is fibre textured. This is in agreement with the findings of the global texture measurements. Furthermore it is apparent that the c -axis of the abnormally large grains has a very good alignment parallel to the out of plane direction while the surrounding smaller grains tend to exhibit a higher degree of misorientation. In this context the results of global texture measurements seems to be in contradiction to the local texture observations, as Magnet A shows the better fibre texture while it contains a lower number of well aligned abnormal large grains. However, that grains represent less than 2% of the microstructure and do not influence the global texture, which is mainly controlled by the alignment of the fine grained majority. As this grains are better

aligned in Magnet A this sample shows an enhanced fibre texture.

The remarkably good alignment of the abnormal grains can be explained as follows. During the alignment of the initial powder under the application of a magnetic field, H , a torque, L , acts on an unaligned spherical particle with magnetic moment, m , and misalignment angle, φ :

$$L = \mu_0 \cdot m \cdot H \cdot \sin \varphi \quad (1)$$

This torque raises the potential energy of the particle, E_{pot} , for its given misalignment:

$$E_{pot} = \mu_0 \cdot m \cdot H \cdot (1 - \cos \varphi) \quad (2)$$

Under the action of the applied field, the particle will reduce its misalignment in order to reduce the potential energy. The rotation of the particle to reduce φ is hindered by the friction between the particle and its neighbourhood and the friction work, W_F , which has to be done to align a particle is equal to

$$W_F = F_f \cdot r \cdot \varphi \quad (3)$$

Besides the particle radius, r , and the misalignment angle, the friction work depends on the friction force which can be approximated as the sum of the particle-particle contact forces between one particle and its neighbours [52]. Assuming all particles have the same size, the number of neighbours of each particle should be independent of the particle radius. The friction force between one particle and its neighbours is therefore also independent of the radius.

For the equilibrium condition $E_{pot}=W_f$ a misalignment angle φ_{eq} is defined, which can be interpreted as follows. For particles with an initial misorientation $\varphi > \varphi_{eq}$ the particle will align its magnetically easy axis during a rigid body rotation under the action of the applied magnetic field until the condition $\varphi=\varphi_{eq}$ is reached. A further reduction of φ is not possible. Particles with initial misorientation angles $\varphi < \varphi_{eq}$ cannot be rotated toward smaller misorientations under the applied field alignment since the friction work during alignment will always be larger than the reduction of the potential energy.

The equilibrium angle φ_{eq} is inversely proportional to the magnetic moment of the particle which is itself proportional to the particle volume. For spherical particles the following relationship is obtained¹:

$$\varphi_{eq} \sim \frac{1}{r^2} \quad (4)$$

From Eq. (4) it is visible that a particle size dependent angle exists, which defines the maximum misorientation of a selected particle size, but not all grains of this size have this maximum misorientation angle but rather the orientation of the grains is statistically distributed. Larger grains in a particle size distribution will therefore tend to be aligned better. If these grains are above the critical size, abnormal grain growth may occur during sintering resulting in abnormal grains with well aligned *c*-axis. This is in good agreement with the results of the microtexture investigations in Fig. 6(a) and (c). Furthermore the better crystallographic texture in Magnet A can be explained by the normal grain growth which occurs homogeneously in the microstructure. In this case the smallest grains with the largest misorientation are consumed by surrounding grains with slightly larger diameter and better crystallographic alignment. This possible mechanism to increase the crystallographic texture during sintering was also discussed elsewhere [53].

3.3. Impact of microstructure on magnetic properties

The demagnetisation curve for both magnets is shown in Fig. 7. Magnet A shows a rectangular demagnetisation curve with remanence $J_r=1.368$ T and coercivity $H_{cJ}=1434$ kA/m resulting in an energy product $(BH)_{max}=367$ kJ/m³. Magnet B shows a coercivity of more than 1600 kA/m. The higher RE content which was necessary to reach full density during the sintering causes a reduction of J_r to 1.272 T which consequently also reduces $(BH)_{max}$ to 313 kJ/m³. The most significant feature of the demagnetisation curve of Magnet B is the greatly reduced rectangularity compared to Magnet A. The rectangularity can be quantified by the ratio $H_{D2}:H_c$. H_{D2} corresponds to the applied magnetic field at which the remanent polarisation is reduced by 2%, which is equivalent to 1% of the volume of the magnet switching its polarisation. For a perfect rectangular demagnetisation curve this ratio would be 1, which is almost the case for Magnet A ($H_{D2}/H_c=0.93$) but the value for Magnet B is much lower ($H_{D2}/H_c=0.68$).

The microstructure of Magnet B consists approximately 2 vol% of abnormal grains. The presence of abnormal grains has been shown to reduce coercivity [21,23] as well as rectangularity [7,8,22]. Ramesh et al. demonstrated the influence of different volume fractions of large grains on the shape of the demagnetisation curve and they found that the presence of a few percentage of large grains is sufficient to deteriorate the rectangularity substantially [8]. Furthermore it was noticed that a kink which is attributed to the switching of abnormal large grains is not always visible in the demagnetisation curve, especially for low volume fractions of abnormal large grains. This is similar to other published results [7,8,54].

The demagnetisation behaviour of Nd-Fe-B sintered magnets is controlled by the nucleation of reversal domains which takes place

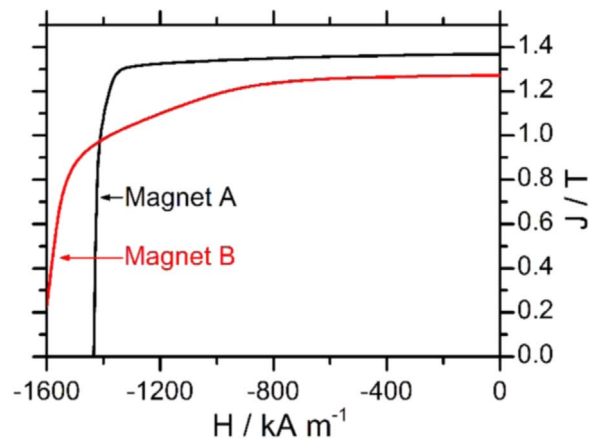


Fig. 7. Demagnetisation curve of Magnet A (black line) and Magnet B (red line). (For interpretation of the references to color in this figure legend, the reader is referred to the web version of this article.)

preferentially at the grain surface and once a reversal domain has nucleated the magnetisation of the whole grain switches rapidly. The probability to find a critical defect which promotes the formation of a reversal domain at low demagnetising field depends on the grain size [7]. The abnormal grains, therefore show a lower nucleation field compared to the fine grained matrix. In the plane of the EBSD map in Fig. 6(c) and (d), the abnormal grain has 74 neighbouring small grains while the small grains have on average only 5 neighbours. In 3D the number of neighbours is of course higher. For the largest abnormal grains observed here, with diameters of ≥ 50 μ m, more than 5000 neighbouring fine grains might be expected. It seems to be possible that the reversing event of an abnormal grain could influence its neighbourhood, e.g. the fine-grained matrix, due to magnetostatic interaction. This could result in a local increase of the demagnetising field acting on a small grain due to the superposition of the external field and a contribution from the stray field of the reversed abnormal grain.

Furthermore the degree of crystallographic texture is lower in Magnet B and this will also contribute to a reduced rectangularity. The impact of reduced texture should be only of minor importance since this magnet still has a strong degree of fibre texture.

The different (de-)magnetisation behaviour can be visualized using the magneto-optical Kerr effect [55–57]. Fig. 8 shows the above mentioned abnormally large grains in Kerr contrast. The angle in each picture indicates the direction of the applied field with 0° pointing upwards and 180° pointing downwards. The sample is oriented with the easy axis pointing out of the plane. Three grains are marked in the first image: The largest grain exhibits a star-like domain pattern indicating that the *c*-axis of the grain is pointing out of the plane, like in the majority of the sample. The second grain adjacent to the lower right shows much broader, stripe like domains, which indicate a large misorientation angle. The smallest grain is marked to represent the majority of small grains in the sample. These three grains behave differently when the applied field is turned. In the largest grain the domain pattern changes as some domains grow and move through the sample. At a rotation angle of 60° the domain pattern is evenly developed throughout the whole grain but it vanishes almost completely at 120° to be formed again at 180°. The stripe domains of the misoriented, large grain vanish almost instantly to be formed again close to 180°. Both large grains invert their domain contrast completely showing that the magnetisation of the grains was reversed. In the smallest grain the domains are moved a little by the rotated field, but they are not affected as drastically as in the large grains and no magnetisation reversal is observable. This shows that a field of about 1 T applied perpendicular to the easy axis is already sufficient to achieve magnetisation reversal in the large grains at the surface whereas the small ones exhibit a larger resistance against magnetisa-

¹Note that the relationship can be obtained if the series expansion $\cos x = 1 - \frac{1}{2!}x^2 + \frac{1}{4!}x^4 - \dots$ is used up to the second term. This approximation may be valid for misorientation angles smaller than 45°.

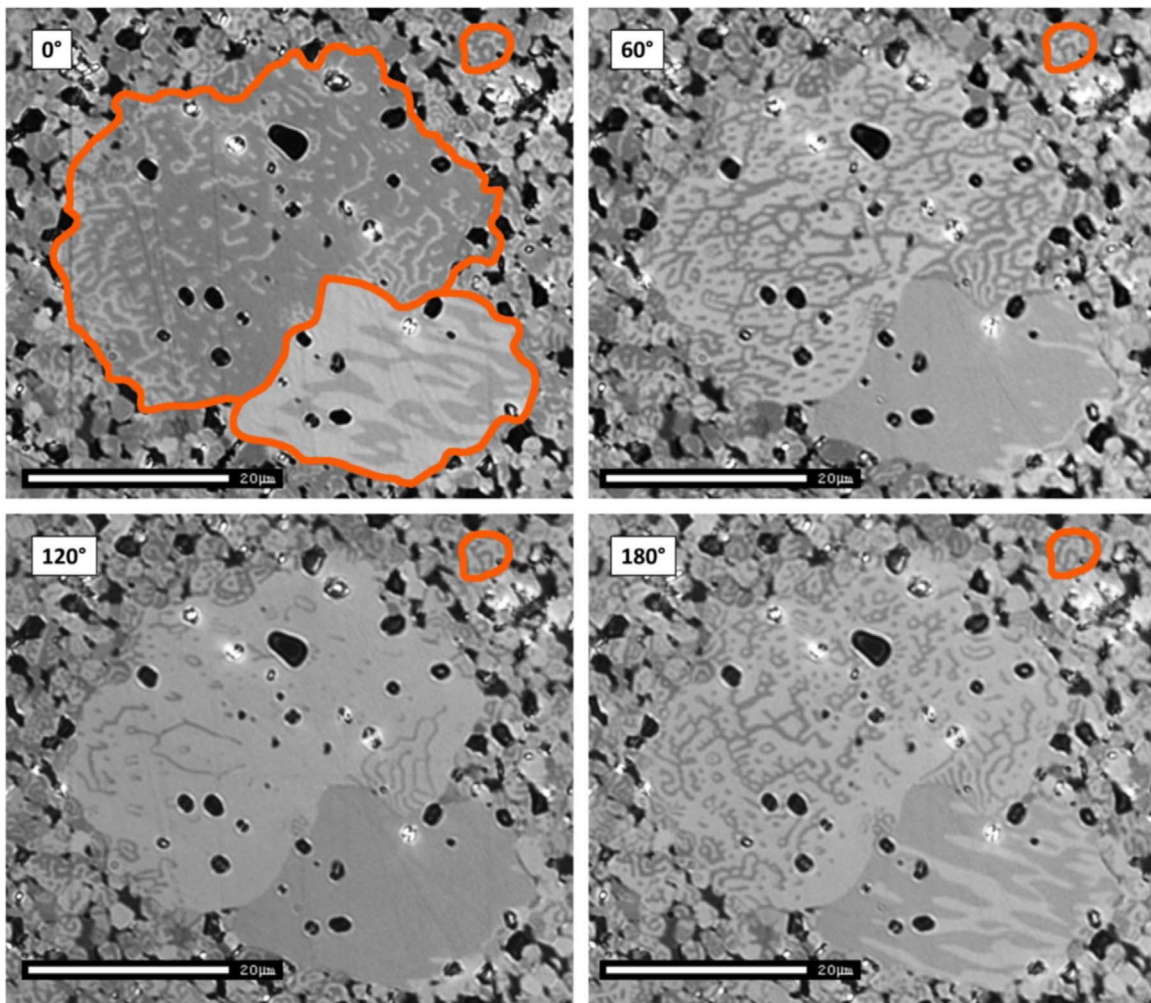


Fig. 8. Light microscope images with Kerr contrast and an in-plane field with the indicated rotation angle for Magnet B.

tion reversal.

The large grains and even some of the small grains change their magnetisation at a much lower field than indicated by the coercivity and the magnetisation curves of the sample. This is related to the limitations of the MOKE measurement as it is only possible to observe surface grains. These grains are affected by the polishing process which results in a large amount of nucleation sites. The demagnetisation factor is also influenced as the geometry of the grains is changed. Both factors lead to a reduced coercivity in the observed surface grains and enable magnetisation reversal at a lower applied field as compared to the macroscopic coercivity as measured in M-H-loops of macroscopic samples [58].

In any case the results from the MOKE measurements support the conclusion that the presence of abnormal large grains can be one cause of the reduced rectangularity as they switch their magnetisation at lower fields than the small grains which represent the majority of the sample.

Fig. 9 shows the dependence of coercivity on the average grain size for both magnets (displayed as stars) and furthermore the results of the study by Uestuener et al. [11] (displayed as circles) for comparison. Uestuener et al. fitted their results to a polynomial function $H_c = 2160 \frac{kA}{m \mu m} \cdot d^{-0.4}$ which is also shown in Fig. 9 as dashed line. A maximum coercivity of 1178 kA/m was obtained for an HRE free sintered magnet with a mean grain size of 3.8 μm. In the present study, the average grain size was reduced below 2 μm and coercivity was enhanced by 21% for Magnet A and 36% for Magnet B without the usage of any HRE elements.

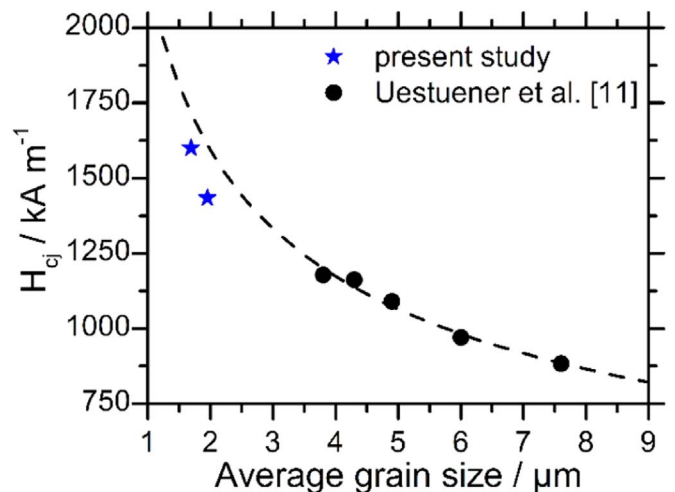


Fig. 9. Coercivity of the sintered magnets in dependence on the average grain size in comparison with the results of Uestuener et al. [11]. The potential regression is shown as dashed line.

It can be concluded from Fig. 9 that the major contribution for increasing coercivity comes from the reduction of the average grain size below 2 μm and that the magnets of the present study follow the predicted trend reasonably well. The deviations from the trend line can be explained by differences in composition between the magnets used here and those studied by Uestuener et al. [11]. Magnet B lies closer to

the trend line than Magnet A, which may be explained by the higher RE content of Magnet B resulting in a better covering of the 2:14:1 grains by the Nd-rich grain boundary phase. This would reduce the number of potential nucleation sites of reversal domains and cause therefore a higher nucleation field.

4. Conclusions

Fine-grained sintered magnets with compositions $(\text{Nd,Pr})_{14.99}\text{Fe}_{76.05}\text{TM}_{3.25}\text{B}_{5.71}$ and $(\text{Nd,Pr})_{17.02}\text{Fe}_{74.18}\text{TM}_{3.19}\text{B}_{5.61}$ (Magnet A and B, TM=Co, Al, Ga) were produced from He jet milled powders by low temperature sintering.

The average grain size of the magnets, measured using the linear intercept method, was 1.95 μm and 1.69 μm for Magnet A and Magnet B, respectively. The slightly larger grain size of Magnet A is attributed to normal grain growth occurring at the higher sintering temperature (cf. 980 °C for Magnet A and 920 °C for Magnet B). TEM showed that both magnets exhibited continuous, Nd-rich intergranular phases of approx. 3 nm in thickness. The composition of the intergranular and grain boundary junction phases were similar to those found in conventional sintered magnets.

Abnormal grain growth was found in both samples and the number and area fraction of abnormal grains was higher in Magnet B. Abnormal grain growth was not expected in these materials since it usually requires a certain critical temperature to be exceeded and no previous reports of abnormal grain growth below a sintering temperature of 1000 °C exist for Nd-Fe-B sintered magnets. Kerr microscopy showed that the abnormal grains had a much lower switching field than the fine-grained matrix.

The microtexture investigations using EBSD showed a better crystallographic alignment of the abnormal grains compared to the fine-grained matrix. This can be explained by a particle size dependent alignment of the powder particles before sintering. Particles with a diameter larger than the average size will tend to be better aligned under magnetic field compared to smaller particles. If these large grains exceed a critical size abnormal growth may occur during sintering. The orientation of the grain is unchanged during abnormal grain growth. The global crystallographic texture was determined using the EBSD sampling method and strong $\langle 001 \rangle$ fibre texture was found in both magnets. The degree of texture is higher in Magnet A, probably because normal grain growth occurred in this sample, which resulted in the removal of the smallest, least well oriented grains from the microstructure.

The room temperature coercivities of the fine-grained magnets are 1434 kA/m and > 1600 kA/m for Magnet A and Magnet B, respectively, which are substantially higher than that of sintered magnets prepared from N_2 Jet milled powders where a coercivity of 1178 kA/m was obtained for a grain size of 3.8 μm [11]. The higher content of abnormal large grains with low switching field and, as a smaller contribution, the reduced crystallographic texture caused a deterioration of the rectangularity of the demagnetisation curve in Magnet B. Microstructural refinement shows a large potential to produce magnets with enhanced coercivity without the usage of HRE elements but new processing strategies must be developed to inhibit abnormal as well as homogenous grain growth at low sintering temperatures.

Acknowledgement

The authors thank Dr. J. Thielsch, T.Mix, A. Chirkova and K. Berger for experimental assistance and Dr. K.-H Müller (all at IFW Dresden) for helpful discussions. TEM investigation was carried out using facilities at USTEM, TU Wien. Kerr microscopy was carried out at TU Darmstadt. The work was partially financed by the FP7 EU project Replacement and Original Magnet Engineering Options (ROME0) (Grant no. 309729).

References

- [1] O. Gutfleisch, M.A. Willard, E. Brück, C.H. Chen, S.G. Sankar, J.P. Liu, Magnetic materials and devices for the 21st century: stronger, lighter, and more energy efficient, *Adv. Mater.* 23 (2011) 821–842.
- [2] K. Hono, H. Sepehri-Amin, Strategy for high-coercivity Nd-Fe-B magnets, *Scr. Mater.* 67 (2012) 530–535.
- [3] R. Skomski, J.M.D. Coey, *Permanent Magnetism*, Institute of Physics Publishing, Bristol and Philadelphia, 1999.
- [4] M. Sagawa, K. Hiraga, H. Yamamoto, Y. Matsuura, Permanent magnet materials based on the rare earth-iron-boron tetragonal compounds (invited), *IEEE Trans. Magn.* 20 (1984) 1584–1589.
- [5] European Commission, Report on Critical Raw Materials for the EU: Critical Raw Materials Profiles, 2014. (http://ec.europa.eu/growth/sectors/raw-materials/specific-interest/index_en.htm).
- [6] S. Massari, M. Ruberti, Rare earth elements as critical raw materials: focus on international markets and future strategies, *Resour. Policy* 38 (2013) 36–43.
- [7] R. Ramesh, K. Srikrishna, Magnetization reversal in nucleation controlled magnets. I. Theory, *J. Appl. Phys.* 64 (1988) 6406–6415.
- [8] R. Ramesh, G. Thomas, B.M. Ma, Magnetization reversal in nucleation controlled magnets. II. Effect of grain size and size distribution on intrinsic coercivity of Fe-Nd-B magnets, *J. Appl. Phys.* 64 (1988) 6416–6423.
- [9] S. Hirotsawa, On the dependence of intrinsic coercivity on grain size in the nucleation-controlled rare earth-iron-boron sintered magnets, *IEEE Trans. Magn.* 25 (1989) 3437–3439.
- [10] P. Nothnagel, K.H. Mueller, D. Eckert, A. Handstein, The influence of particle size on the coercivity of sintered NdFeB magnets, *J. Magn. Magn. Mater.* 101 (1991) 379–381.
- [11] K. Uestuener, M. Katter, W. Rodewald, Dependence of the mean grain size and coercivity of sintered Nd-Fe-B magnets on the initial powder particle size, *IEEE Trans. Magn.* 42 (2006) 2897–2899.
- [12] W.F. Li, T. Ohkubo, K. Hono, M. Sagawa, The origin of coercivity decrease in fine grained Nd-Fe-B sintered magnets, *J. Magn. Magn. Mater.* 321 (2009) 1100–1105.
- [13] M.H. Prahl, *Zerkleinerungstechnik*, Verlag TÜV Rheinland, 1991.
- [14] H. Sepehri-Amin, Y. Une, T. Ohkubo, K. Hono, M. Sagawa, Microstructure of fine-grained Nd-Fe-B sintered magnets with high coercivity, *Scr. Mater.* 65 (2011) 396–399.
- [15] Y. Une, M. Sagawa, Enhancement of coercivity of Nd-Fe-B sintered magnets by grain size reduction, *J. Jpn. Inst. Met.* 76 (2012) 12–16.
- [16] K. Hono, T. Ohkubo, H. Sepehri-Amin, Microstructure-coercivity relationships of Nd-Fe-B base permanent magnets, *J. Jpn. Inst. Met.* 72 (2012) 2–11.
- [17] M. Sagawa, S. Hirotsawa, H. Yamamoto, S. Fujimura, Y. Matsuura, Nd-Fe-B permanent magnet materials, *Jpn. J. Appl. Phys.* 26 (1987) 785–800.
- [18] W. Rodewald, B. Wall, W. Fernengel, Grain growth kinetics in sintered Nd-Fe-B Magnets, *IEEE Trans. Magn.* 33 (1997) 3841–3843.
- [19] W. Rodewald, B. Wall, M. Katter, K. Uestuener, Topology of Nd-Fe-B magnets with a high energy density, *IEEE Trans. Magn.* 39 (2003) 2932–2934.
- [20] N.C. Liu, a.S. Kim, Abnormal grain growth in sintered Nd-Fe-B magnets, *J. Appl. Phys.* 67 (1990) 4629–4631.
- [21] Y. Kaneko, K. Tokuhara, N. Ishigaki, Research on high performance magnets sintered, *Vacuum* 47 (1996) 907–910.
- [22] S. Sasaki, J. Fiedler, M. Sagawa, High Performance sintered Nd-Fe-B magnets made by new RIP from SC alloys, in: Proceedings 16 International Workshop Rare-Earth Magnets Their Applications, 2000, pp. 109–118.
- [23] A.S. Kim, Magnetic properties of sintered Nd-Fe-B magnets from hydrided materials, *J. Appl. Phys.* 70 (1991) 6462–6464.
- [24] J.-M. Missiaen, G. Richard, C.H. Allibert, F. Vial, Normal and Abnormal Grain Growth in Nd-Fe-B Sintered Magnets, *World Congr. Powder Metall.* (1998) 636–641.
- [25] F. Vial, E. Rozendaal, M. Sagawa, Improvement of the Microstructure and Magnetic Properties of Sintered NdFeB Permanent Magnets, in: Proceedings 10 International Workshop Rare-Earth Magnets Their Applications, 1998: pp. 401–410.
- [26] S. Namkung, D.H. Kim, T.S. Jang, Effect of particle size distribution on the microstructure and magnetic properties of sintered NdFeB magnets, *Rev. Adv. Mater. Sci.* 28 (2011) 185–189.
- [27] J.F. Herbst, R2Fe14B materials: intrinsic properties and technological aspects, *Rev. Mod. Phys.* 63 (1991) 819–898.
- [28] K. Detert, Secondary Recrystallization, in: F. Haessner (Ed.), *Recryst. Met. Mater., Dr. Riedener-Verlag GmbH, Stuttgart*, 1978, pp. 97–109.
- [29] O. Isnard, W.B. Yelon, S. Miraglia, D. Fruchart, Neutron-diffraction study of the insertion scheme of hydrogen in Nd 2Fe14B, *J. Appl. Phys.* 78 (1995) 1892–1898.
- [30] P. Villars, L.D. Calvert, *Pearson's Handbook of Crystallographic Data for Intermetallic Phases*, 2nd ed., ASM International, Materials Park, OH, 1991.
- [31] J.M. Leger, N. Yacoubi, J. Loriers, Synthesis of rare earth monoxides, *J. Solid State Chem.* 36 (1981) 261–270.
- [32] J. Fidler, Analytical microscope studies of sintered Nd-Fe-B magnets, *IEEE Trans. Magn.* 21 (1985) 1955–1957.
- [33] D. Lemarchand, P. Vigier, B. Labulle, On the oxygen stabilized Nd-rich phase in the Nd-Fe-B (-O) permanent magnet system, *IEEE Trans. Magn.* 26 (1990) 2649–2651.
- [34] W. Tang, S. Zhou, R. Wang, C.D. Graham, An investigation of the Nd-rich phases in the Nd-Fe-B system, *J. Appl. Phys.* 64 (1988) 5516–5518.
- [35] J. Fidler, K.G. Knoch, Electron-microscopy of Nd-Fe-B based magnets, *J. Magn. Magn. Mater.* 80 (1989) 48–56.

- [36] S.C. Wang, Y. Li, In situ TEM study of Nd-rich phase in NdFeB magnet, *J. Magn. Magn. Mater.* 285 (2005) 177–182.
- [37] G. Hrkac, T.G. Woodcock, K.T. Butler, L. Saharan, M.T. Bryan, T. Schrefl, O. Gutfleisch, Impact of different Nd-rich crystal-phases on the coercivity of Nd-Fe-B grain ensembles, *Scr. Mater.* 70 (2014) 35–38.
- [38] T.G. Woodcock, O. Gutfleisch, Multi-phase EBSD mapping and local texture analysis in NdFeB sintered magnets, *Acta Mater.* 59 (2011) 1026–1036.
- [39] J. Fidler, J. Bernardi, T. Schrefl, Permanent magnets – new microstructural aspects, *Scr. Metall. Mater.* 33 (1995) 1781–1791.
- [40] D. Drouin, A.R. Couture, D. Joly, X. Tastet, V. Aimez, R. Gauvin, CASINO V2.42—a fast and easy-to-use modeling tool for scanning electron microscopy and micro-analysis users, *Scanning* 29 (2007) 92–101.
- [41] R.F. Egerton, *Electron Energy-Loss Spectroscopy in the Electron Microscope*, 2nd ed., Plenum Press, New York, 1996.
- [42] H. Sepehri-Amin, T. Ohkubo, T. Shima, K. Hono, Grain boundary and interface chemistry of an Nd-Fe-B-based sintered magnet, *Acta Mater.* 60 (2012) 819–830.
- [43] T.T. Sasaki, T. Ohkubo, Y. Ue, H. Kubo, M. Sagawa, K. Hono, Effect of carbon on the coercivity and microstructure in fine-grained Nd–Fe–B sintered magnet, *Acta Mater.* 84 (2015) 506–514.
- [44] T.G. Woodcock, Q.M. Ramasse, G. Hrkac, T. Shoji, M. Yano, A. Kato, O. Gutfleisch, Atomic-scale features of phase boundaries in hot deformed Nd-Fe-Co-B-Ga magnets infiltrated with a Nd-Cu eutectic liquid, *Acta Mater.* 77 (2014) 111–124.
- [45] K. Kobayashi, K. Urushibata, T. Matsushita, S. Sakamoto, S. Suzuki, Magnetic properties and domain structures in Nd-Fe-B sintered magnets with Tb additive reacted and diffused from the sample surface, *J. Alloy. Compd.* 615 (2014) 569–575.
- [46] Y. Murakami, T. Tanigaki, T.T. Sasaki, Y. Takeno, H.S. Park, T. Matsuda, et al., Magnetism of ultrathin intergranular boundary regions in Nd–Fe–B permanent magnets, *Acta Mater.* 71 (2014) 370–379.
- [47] G.A. Zickler, P. Toson, A. Asali, J. Fidler, Nanoanalytical TEM Studies and Micromagnetic Modelling of Nd-Fe-B Magnets, *Phys. Procedia* 75 (2015) 1442–1449.
- [48] P. Toson, G.A. Zickler, J. Fidler, Do micromagnetic simulations correctly predict hard magnetic hysteresis properties?, *Phys. B Condens. Matter* (2015) 1–9.
- [49] G.A. Zickler, J. Fidler, J. Bernardi, T. Schrefl, A. Asali, A combined TEM/STEM and micromagnetic study of the anisotropic nature of grain boundaries and coercivity in Nd-Fe-B magnets, *Adv. Mater. Sci. Eng.* (11/2016) In review.
- [50] S.I. Wright, M.M. Nowell, J.F. Bingert, A comparison of textures measured using X-ray and electron backscatter diffraction, *Metall. Mater. Trans. A* 38 (2007) 1845–1855.
- [51] S. Sawatzki, T.G. Woodcock, K. Güth, K.-H. Müller, O. Gutfleisch, Calculation of remanence and degree of texture from EBSD orientation histograms and XRD rocking curves in Nd–Fe–B sintered magnets, *J. Magn. Magn. Mater.* 382 (2015) 219–224.
- [52] D. Schulze, *Pulver und Schüttgüter*, 2nd ed., Springer-Verlag, Berlin, Heidelberg, 2009.
- [53] W.C. Chang, T.B. Wu, K.S. Liu, A texture study of anisotropic sintered Nd-Fe-B magnets, *J. Appl. Phys.* 63 (1988) 3531–3533.
- [54] M.R. Corfield, I.R. Harris, a.J. Williams, Influence of oxygen content on grain growth in Pr–Fe–B/Nd–Fe–B sintered magnets, *J. Alloy. Compd.* 463 (2008) 180–188.
- [55] A. Hubert, R. Schäfer, *Magnetic Domains*, Springer-Verlag, Berlin, Heidelberg, 1998.
- [56] O. Gutfleisch, D. Eckert, R. Schäfer, K.-H. Müller, V. Panchathan, Magnetization processes in two different types of anisotropic, fully dense NdFeB hydrogenation, disproportionation, desorption, and recombination magnets, *J. Appl. Phys.* 87 (2000) 6119–6121.
- [57] K. Khlopkov, O. Gutfleisch, D. Eckert, D. Hinz, B. Wall, W. Rodewald, K.-H. Müller, L. Schultz, Local texture in Nd-Fe-B sintered magnets with maximised energy density, *J. Alloy. Compd.* 365 (2004) 259–265.
- [58] T.G. Woodcock, Y. Zhang, G. Hrkac, G. Ciuta, N.M. Dempsey, T. Schrefl, O. Gutfleisch, D. Givord, Understanding the microstructure and coercivity of high performance NdFeB-based magnets, *Scr. Mater.* 67 (2012) 536–541.